ACCOUNTS of chemical research

Article

Cite This: *Acc. Chem. Res.* 2018, 51, 3144−3153

pubs.acs.org/accounts

Emerging Design and Characterization Guidelines for Polymer-Based Infrared Photodetectors

Published as part of the Accounts of Chemical Research special issue "Wearable Bioelectronics: Chemistry, Materials, Devices, and Systems".

Zhenghui Wu,[†] Yichen Zhai,[†] Hyonwoong Kim,[†] Jason D. Azoulay,[‡] and Tse Nga Ng*,[†]

[†]Department of Electrical and Computer Engineering, University of California San Diego, 9500 Gilman Drive, La Jolla, California 92093-0407, United States

[‡]School of Polymer Science and Engineering, The University of Southern Mississippi, 118 College Drive #5050, Hattiesburg, Mississippi 39406, United States

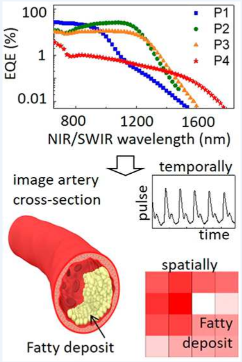

CONSPECTUS: Infrared photodetectors are essential to many applications, including surveillance, communications, process monitoring, and biological imaging. The short-wave infrared (SWIR) spectral region (λ = 1−3 μm) is particularly powerful for health monitoring and medical diagnostics because biological tissues show low absorbance and minimal SWIR autofluorescence, enabling greater penetration depth and improved resolution in comparison with visible light. However, current SWIR photodetection technologies are largely based on epitaxially grown inorganic semiconductors, which are costly, require complex processing, and impose cooling requirements incompatible with wearable electronics. Solution-processable semiconductors are being developed for infrared detectors to enable low-cost direct deposition and facilitate monolithic integration and resolution not achievable using current technologies. In particular, organic semiconductors offer numerous advantages, including large-area and conformal coverage, temperature insensitivity, and biocompatibility, for enabling ubiquitous SWIR optoelectronics.

This Account introduces recent efforts to advance the spectral response of organic photodetectors into the SWIR. High-performance visible to near-infrared (NIR) organic photodetectors have been demonstrated by leveraging the wealth of knowledge from organic solar cell research in the past decade. On the other hand, organic semiconductors that absorb in the SWIR are just emerging, and only a few organic materials have been reported that exhibit photocurrent past 1 μm. In this Account, we survey novel SWIR molecules and polymers and discuss the main bottlenecks associated with charge recombination and trapping, which are more challenging to address in narrow-band-gap photodetectors in comparison with devices operating in the visible to NIR. As we call attention to discrepancies in the literature regarding performance metrics, we share our perspective on potential pitfalls that may lead to overestimated values, with particular attention to the detectivity (signal-to-noise ratio) and temporal characteristics, in order to ensure a fair comparison of device performance.

As progress is made toward overcoming challenges associated with losses due to recombination and increasing noise at progressively narrower band gaps, the performance of organic SWIR photodetectors is steadily rising, with detectivity exceeding 10^{11} Jones, comparable to that of commercial germanium photodiodes. Organic SWIR photodetectors can be incorporated into wearable physiological monitors and SWIR spectroscopic imagers that enable compositional analysis. A wide range of potential applications include food and water quality monitoring, medical and biological studies, industrial process inspection, and environmental surveillance. There are exciting opportunities for low-cost organic SWIR technologies to be as widely deployable and affordable as today's ubiquitous cell phone cameras operating in the visible, which will serve as an empowering tool for users to discover information in the SWIR and inspire new use cases and applications.

1. INTRODUCTION

Optical sensors are essential in wearable electronics that enable health monitoring, telemedicine, and biological studies. While today's photodetectors primarily transduce visible light (wavelength (λ) = 0.4−0.7 μm) and near-infrared (NIR) radiation (λ = 0.7−1 μm), there are significant advantages in extending the detection window into the short-wave infrared (SWIR) region (λ = 1−3 μm), including low tissue absorbance and minimal autofluorescence, which greatly improve the detection depth and resolution.[1,2] While SWIR detection is highly desirable, crystalline infrared devices remain expensive because of fabrication and cooling requirements that are incompatible with wearable systems.

This Account surveys recent efforts to advance the photoresponse of organic SWIR devices to enable cost-effective infrared detectors. In addition to the ease of solution processing,[3,4] organic molecules and polymers offer excellent

Received: September 4, 2018
Published: December 6, 2018

DOI: 10.1021/acs.accounts.8b00446

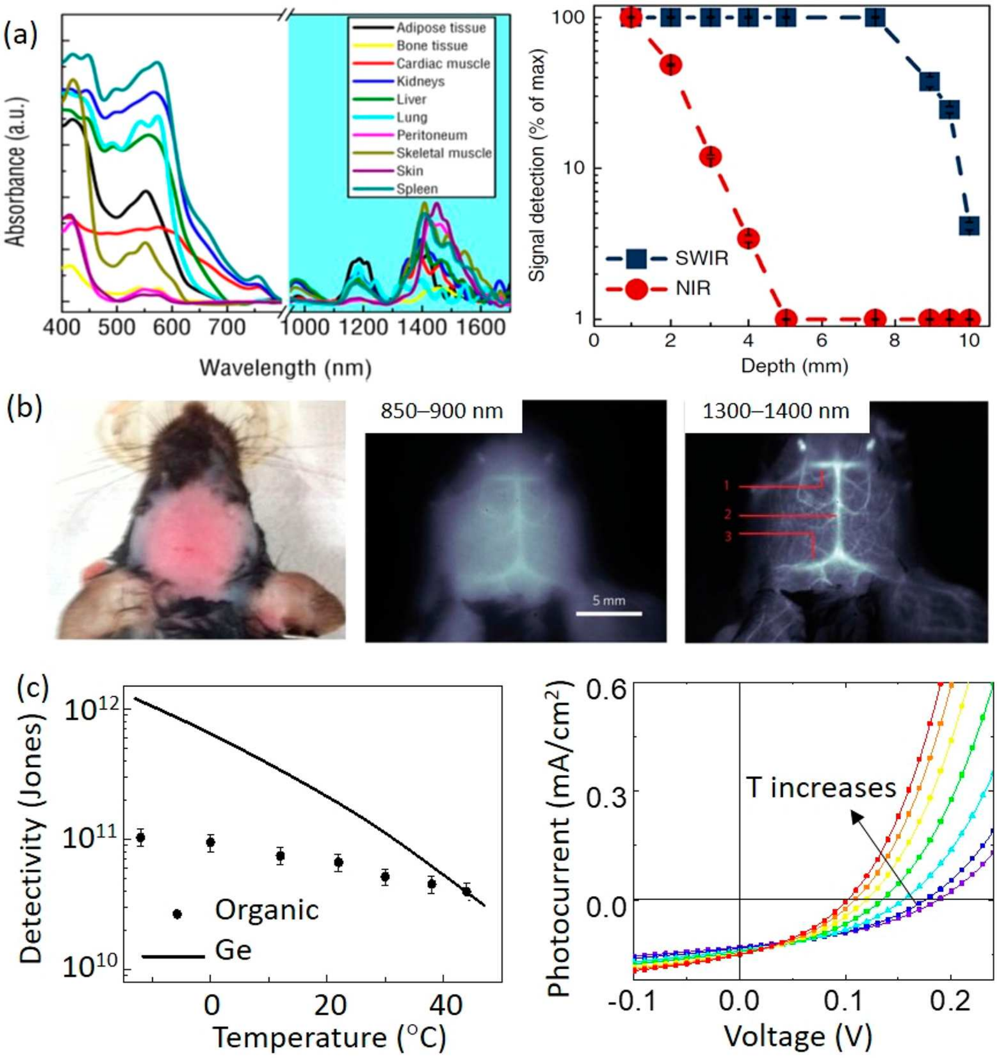

Figure 1. (a) Absorbance of biological tissues vs spectral wavelength (left) and light penetration at 808 nm (NIR) or at 1525 nm (SWIR) vs the tissue phantom depth (right). Reproduced with permission from ref 1. Copyright 2013 Nature Publishing Group. (b) Comparison of noninvasive fluorescence imaging of a mouse brain in different spectral regions. Reproduced with permission from ref 2. Copyright 2014 Nature Publishing Group. (c) Comparison of the detectivities as functions of temperature for a commercial germanium photodiode and a typical organic photodiode (left) and photocurrent−voltage characteristics as the temperature is varied from −12 to 48 °C (right). Reproduced from ref 24. Copyright 2016 American Chemical Society.

mechanical flexibility[5−8] and biocompatibility,[9] which render them particularly suitable for wearable optoelectronic applications.[10−13] Despite the demonstrated performance of organic semiconductors in the visible and NIR, organic semiconductors that absorb in the SWIR are just emerging, and only a few materials exhibit photocurrent past 1 μm.[14−20] Thus, there remains a disparity between the limits on the performances of organic photodiodes operating in the SWIR and visible−NIR regions, which is manifested as discrepancies associated with characterization and loss mechanisms seen in the literature.[14−18,21] Here we discuss challenges associated with the implementation of narrow-band-gap polymeric photodetectors and present our characterization guidelines, calling attention to assumptions that potentially overestimate performance metrics such as detectivity and temporal characteristics. Furthermore, we demonstrate examples of biomedical monitoring and address new opportunities using organic SWIR technologies.

2. BIOLOGICAL IMAGING IN THE INFRARED

SWIR imaging benefits from enhanced tissue penetration[1,10] and accuracy,[22,23] as the absorbance of many biological tissues decreases sharply above 700 nm, as shown in Figure 1a.[1] Since photon scattering is inversely proportional to the wavelength, SWIR light penetrates more deeply than NIR light. Figure 1b demonstrates noninvasive fluorescence imaging through an intact mouse skull,[2] in which the contrast and resolution are much higher in the SWIR. These images were acquired with an inorganic InGaAs array, which requires cooling to lower the detector noise. With regard to temperature, organic SWIR semiconductors provide an advantage since they can operate at near-physiological temperatures in wearable electronic platforms. Carrier transport in organics improves with elevated temperature because thermal energy assists carrier hopping. In contrast, carrier transport in crystalline inorganic materials is adversely affected by increasing temperature, as lattice vibrations reduce the mean free path of carriers. Figure 1c highlights that the detectivity, or signal-to-noise ratio, of an

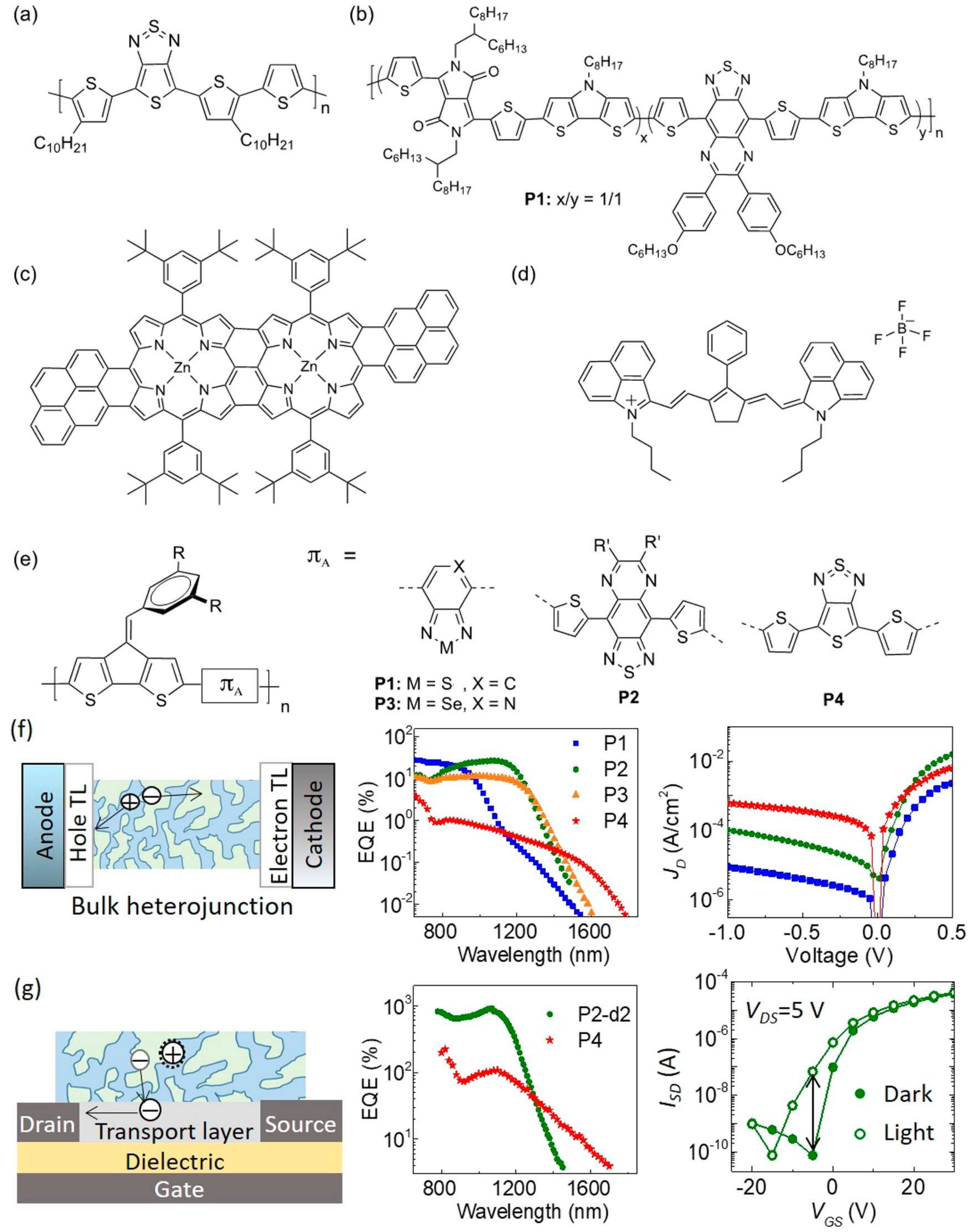

Figure 2. (a−e) Chemical structures of infrared active organic semiconductors.[14−18] (f) Device structure and characteristics of bulk-heterojunction photodiodes. The structures of the polymers used are shown in (e). For P1 and P3, R = $C_{12}H_{25}$. For P4, R = $C_{14}H_{29}$. For P2, R = $OC_{12}H_{25}$, R′ = C_8H_{17}. (g) Device structure of a phototransistor using separate transport and light-sensitized layers (left), external quantum efficiency vs incident wavelength (middle), and transfer characteristics in the dark and under illumination with λ = 940 nm and 17 mW/cm^2 (right). P2-d2 is a derivative of P2 in which R′ = $C_{12}H_{25}$.

organic photodiode is less adversely affected by changes in temperature compared with a germanium photodiode.[24]

3. INFRARED-RESPONSIVE ORGANIC SEMICONDUCTORS AND DEVICE STRUCTURES

Efforts to extend the functionality of organic semiconductors to narrow band gaps (<1.1 eV) have seen a rise in the past decade. The first report of an SWIR-responsive conjugated polymer appeared in 2009.[14] This material, whose structure is shown in Figure 2a, demonstrated a spectral response from 300 to 1450 nm, offering a broadly absorbing alternative to SWIR colloidal quantum dots,[25,26] which are limited to narrow spectral widths by their characteristic zero-dimensional density of states. Another conjugated polymer, shown in Figure 2b, reached a peak external quantum efficiency (EQE) of 8% at 1200 nm with an applied bias of −2 V.[15] The polymer absorption displayed a wide band tail, indicative of high structural disorder resulting in low efficiency. Small molecules, such as the porphyrin dimers in Figure 2c, were explored to reduce disorder and showed EQE = 13% at 1400 nm without an external bias.[16] Heptamethine salts demonstrated absorption out to 1600 nm, but the device EQEs were below 2%.[17] Research in optical management, such as incorporation of microcavities,[27] has been applied to increase the absorption and extend the spectral range. Our team has focused on SWIR polymers, which are amorphous and enable uniform and smooth film deposition. As shown in Figure 2e, the Azoulay lab synthesized a series of donor−acceptor conjugated polymers with variations in the acceptor moieties, which allowed tuning of the semiconductor energy levels.[18] Leveraging this series of materials, the Ng lab demonstrated devices with spectral response up to 1700 nm.[28,29]

Figure 2f displays an organic bulk heterojunction (BHJ) photodiode[30,31] that comprises an SWIR-responsive organic semiconductor used as the p-type donor intermixed with an n-type [6,6]-phenyl-C_{71}-butyric acid methyl ester (PCBM[70]) acceptor. Besides fullerene derivatives, alternative oligomer acceptors designed to improve the device stability and efficiency are emerging.[32,33] The P2 photodiode at 0 V demonstrated[34] a peak EQE of 26%, which is the highest efficiency reported to date for polymeric photodiodes operating without an external bias in the spectral range beyond the cutoff wavelength of silicon at $\lambda = 1100$ nm. As the band gap is reduced in the series of Figure 2e, the spectral response is extended, however, the EQE decreases with a reduction in band gap. The dark current and rectification ratio become worse in moving from the P1 BHJ to the P4 BHJ because of the increasing thermal generation and recombination associated with a decreasing band gap. The concomitant trends of decreasing photoresponse and increasing noise levels with band gap reduction are some of the challenges exemplified in using narrow-band-gap materials.

Another device structure often used in organic photodetectors is the field-effect transistor.[31,35−38] Because of poor charge transport in organic materials, the phototransistor structure is designed with separate channels[38] for charge photogeneration and transport, as shown in Figure 2g. In our bilayer phototransistors, the transport layer consists of indium zinc oxide (IZO),[39] on top of which is the infrared-responsive BHJ. Under illumination, the photogenerated holes are trapped in the polymer, while electrons are transferred to the IZO. The trapped holes induce injection of electrons from the source electrode for the duration of the hole lifetime. The additional injected electrons are instrumental to realize photoconductive gain, enabling the phototransistor EQE to exceed 100%. However, the photoconductive gain mechanism limits the response speed, and thus, there is trade-off between gain and bandwidth. In phototransistors, the difference between the photocurrent and dark current is largest in the subthreshold region, leading to a maximized signal-to-noise ratio, as indicated in Figure 2g.

4. CHALLENGES FACING ORGANIC INFRARED PHOTODETECTORS

Recent characterization and modeling efforts[28,40] have revealed that the probability of recombination increases at progressively narrow band gaps, and therefore, separating the photogenerated excitons into free carriers becomes more challenging. This is in contrast to visible-wavelength organics, which have large band gaps and are not affected as strongly by exciton recombination.[41] In this section, we analyze the bottlenecks of charge recombination and trapping that currently limit SWIR detectivity and speed and also share our perspective on potential pitfalls that lead to overestimation in device characterization. Photodetector metrics relevant to this discussion are defined in Table 1.

4.1. Recombination Across Narrow Band Gaps Affects Signal-to-Noise Ratios

Figure 3a,b illustrates the energy levels and density of states (DOS), respectively, in organic BHJ films. There is strong Coulombic attraction binding the photogenerated singlet excitons (S_1), but the energy offset (ΔE_{LUMO}) at the donor−acceptor interface assists the dissociation of excitons into free electrons and holes. The difference in energy between the highest occupied molecular orbital (HOMO) of the donor and the lowest unoccupied molecular orbital (LUMO) of the acceptor defines the charge-transfer (CT) state, which is the effective band gap (E_{CT}) of the BHJ. When the polymer band gap is wide, the localized band-tail states are well-separated. When the polymer band gap is reduced, the gap between free carriers and trapped charges in localized states becomes small, which increases the probability for electrons and holes to recombine.[42] In comparison with wide-band-gap organics, the band tails of SWIR polymers are empirically more broad and disordered, which further exacerbates efficiency losses due to recombination.

Recombination via localized states affects both the photocurrent and noise levels. Our modeling and experimental results in Figure 3c reveal that this SWIR photodiode is limited by diminished internal electric field, leading to poor dissociation efficiency ($\eta_{\mathrm{dissociate}} \leq 12\%$). Applying an external bias was helpful to increase the photocurrent. However, enhancing the photosignal is just one aspect of device improvement, and the appropriate photodetector metric is the detectivity, or signal-to-noise ratio. Hence, the device noise must be characterized with respect to materials and device parameters, including E_{CT} and the applied bias.

The relation between E_{CT} and the shunt resistance (R_{shunt}) in the dark for our photodiodes is shown in Figure 3d. It can be seen that lower E_{CT} leads to smaller R_{shunt}. The value of R_{shunt} is taken from impedance measurements at low frequency, if the impedance characteristics are not convoluted with interfacial barrier resistance.[43] The range of R_{shunt} is obtained as the BHJ thickness is varied from 150−500 nm, where lower R_{shunt} is attributed to pinholes in thinner films. A further thickness increase did not improve R_{shunt} because of an increased volume for thermal generation of intrinsic carriers. As E_{CT} is reduced, the localized band-tail states are closer in energy, and the intrinsic carriers are thermally excited to nearby band-tail states, contributing to decreasing R_{shunt} and higher thermal noise current. The equation relating R_{shunt} to the thermal noise is included in Table 1. The contribution of thermal noise to the total noise current becomes increasingly large and important in SWIR devices.

Potential Pitfalls in Photodetector Characterization. The total noise spectral density includes components from shot noise (S_{shot}), thermal noise (S_{thermal}), and $1/f$ noise ($S_{1/f}$). In comparison to visible-wavelength photodiodes, thermal generation becomes significant at narrow band gaps, and thermal noise overtakes shot noise near zero bias. However, at high reverse bias, shot noise may dominate again. At a small

Table 1. Definitions of Photodetector Metrics

metric	definition
external quantum efficiency (EQE)	The ratio between the numbers of collected carriers and incident photons: EQE = $(J_{ph}/P_{illumin})(hc/\lambda q)$, where h is Planck's constant, c is the speed of light, λ is the wavelength of the incident light, q is the elementary charge, J_{ph} is the photocurrent density, and $P_{illumin}$ is the intensity of the incident light per unit area. The EQE metric is unitless and often expressed as a percentage.
detectivity (D^*)	The signal-to-noise ratio of responsivity to dark-current noise: $D^* = A^{0.5}R/S_n$, where $R = (J_{ph}/P_{illumin})$ is the responsivity, which is proportional to the EQE at each wavelength, A is the effective photodetector area, and S_n is the noise spectral density of the current. Another view of the detectivity is $D^* = A^{0.5}/\mathrm{NEP}$, i.e., it is the reciprocal of the noise equivalent power (NEP = S_n/R, in units of W/Hz$^{0.5}$) normalized by the area. The unit of D^* is the Jones (1 Jones = 1 cm Hz$^{0.5}$/W).
noise spectral density (S_n)	The noise spectral density of current has multiple components, including shot noise, thermal noise, $1/f$ noise, and potentially others. The total noise is expressed as $S_n = \sqrt{{S_{shot}}^2 + {S_{thermal}}^2 + {S_{1/f}}^2}$. If the detection bandwidth is set to 1 Hz, which is the convention in the community, the shot noise is related to the total current I by $S_{shot@1\,Hz} = \sqrt{2qI}$. The thermal noise is given by $S_{thermal@1\,Hz} = \sqrt{4kT/R_{shunt}}$ where k is Boltzman's constant, T is the temperature, and R_{shunt} is the shunt resistance of the devices. The $1/f$ noise is empirical and often not expressed in terms of device parameters. The unit of S_n is A/Hz$^{0.5}$.

bias of −0.1 mV, $S_{shot}(-0.1\ \mathrm{mV})$ is estimated to be ∼0.02 pA/Hz$^{0.5}$ using the equations in Table 1; this calculated value is an order of magnitude lower than the actual noise measured by a power spectral analyzer or a lock-in amplifier, as shown in Figure 3e. Meanwhile, $S_{thermal}(-0.1\ \mathrm{mV})$ is computed from R_{shunt} and found to be 0.6 pA/Hz$^{0.5}$, which is close to the measured noise. When the reverse bias is increased to −0.5 V, $S_{shot}(-0.5\ \mathrm{V})$ is estimated to be 2 pA/Hz$^{0.5}$, which accounts for the additional noise current displayed as the light-green data. Overall, this analysis emphasizes the importance of direct noise measurements, as the dominant component may change depending on the operational conditions.

An accurate determination of the photodiode detectivity (D^*, the signal-to-noise ratio defined in Table 1) requires proper noise values. However, some publications assume that only shot noise exists and *incorrectly* substitute $\sqrt{2qI_{dark}}$ for the total noise. We caution against this assumption, since we have shown in Figure 3e that shot noise is not necessarily the dominant source, especially in low-band-gap devices. As can be seen in Figure 3f, the detectivity may be overestimated by more than an order of magnitude using the shot noise assumption. Moreover, the detectivity should be experimentally confirmed by showing that the device can detect light on the same order of magnitude as the noise-equivalent power.

For our SWIR photodiodes in Figure 3f, the detectivity is better at zero external bias than under reverse bias. Upon the application of a reverse bias, there is a sharp rise in noise and only a minor improvement in EQE. This characteristic is different from visible photodiodes, where reverse bias does not significantly increase the noise in wider-band-gap materials. The strategies used to raise the detectivity in visible photodiodes, such as increasing the BHJ thickness to reduce the shot noise and applying a high reverse bias to increase EQE, are not applicable to the low-band-gap SWIR devices discussed here[28] because of severe recombination in thick films and substantial noise contributions from band-tail states.

4.2. Trapped Charges Affect the Temporal Responses

Organic SWIR photodiodes typically allow bandwidths of hundreds of kilohertz and stable photocurrent when operated without an external bias. However, there are scenarios where we observe frequency-dependent photocurrent due to a charge extraction barrier at the electrode, as shown in Figure 4a. When there is a mismatched energy level at the interface, the transfer of holes from the BHJ to the anode is slow at this interface bottleneck. As holes gradually accumulate at the interface, they shield and reduce the internal electric field driving charge transport, resulting in a decrease in photocurrent, as shown in Figure 4b, until the charge transport and hole transfer at the interface reach a steady state. Figure 4c compares the EQEs for illumination pulses of different durations, namely, 14 ms (35 Hz at 50% duty cycle) and 1.25 ms (400 Hz at 50% duty cycle). The longer pulse duration allows charge to be trapped at the barrier, reducing the photocurrent with time. Thus, the EQE decreases when the illumination frequency is changed from 400 to 35 Hz. The photocurrent stability is improved when a reverse bias is applied to reduce the extraction barrier. With a reverse bias of −4 V, the photocurrent does not decay with time, and there is no negative peak due to the release of accumulated charge when the light is shut off. Photodiodes with an extraction barrier need to operate at reverse bias to avoid ghosting artifacts, namely, the interference from residual charge from a

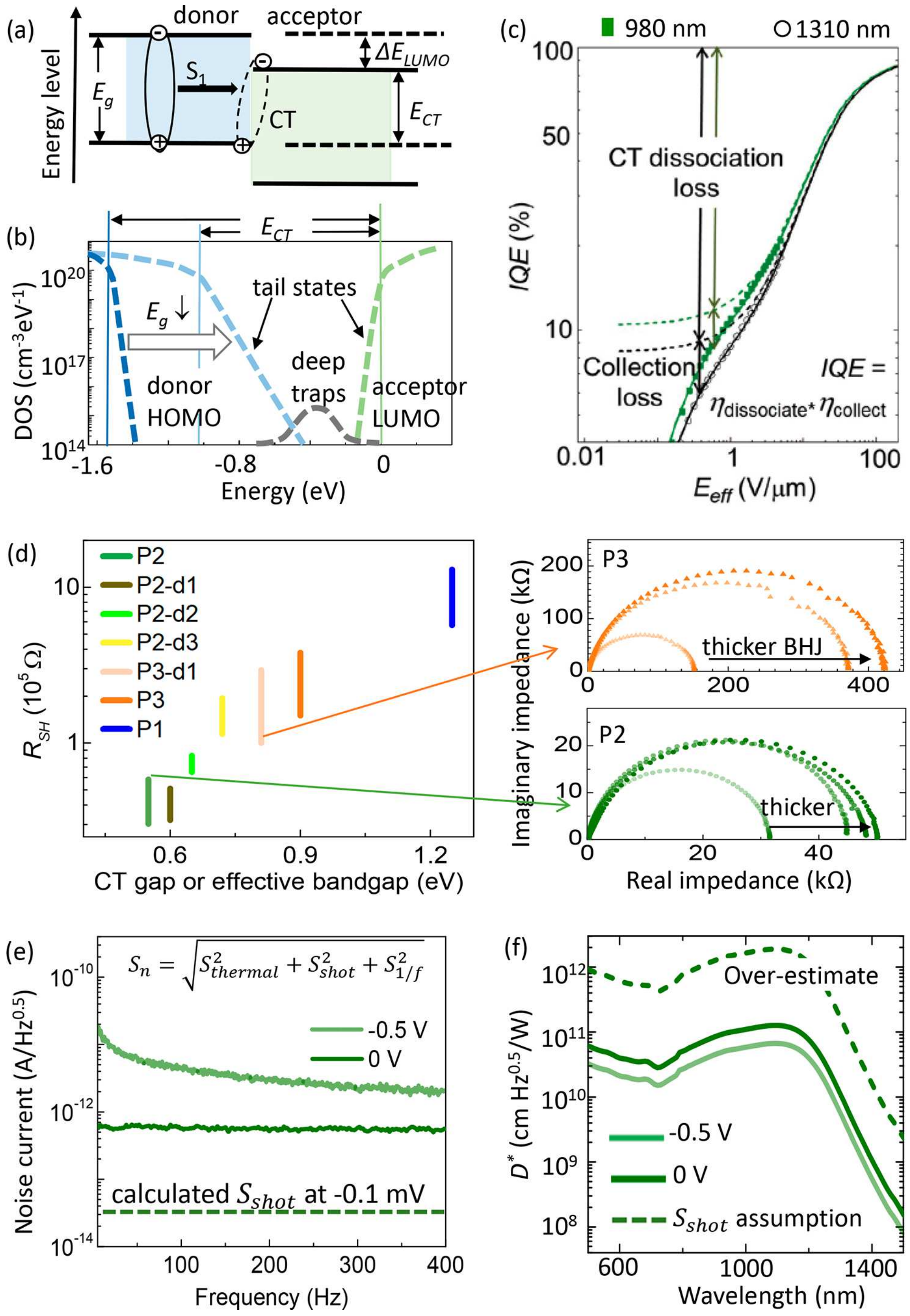

Figure 3. (a) Energy level diagram in a heterojunction film. (b) Reduction of the charge-transfer state (E_{CT}) gap as the polymer band gap (E_g) is decreased. The energy of the acceptor LUMO level is assigned to 0 eV for making convenient comparisons. (c) Internal quantum efficiency (IQE) vs electric field for an organic photodiode under illumination at different wavelengths. Dashed lines represent the theoretical dissociation efficiencies assuming no loss during charge collection. Reproduced with permission from ref 28. Copyright 2018 Wiley. (d) Shunt resistance of organic photodiodes as a function of the E_{CT} for 2:1 blends of PCBM[70] and polymers from Figure 2e. P2-d1, -2, and -3 are derivatives of the P2 polymer, with side chains R′ = $OC_{10}H_{21}$ for d1, $C_{12}H_{25}$ for d2, and $OC_{16}H_{33}$ for d3. P3-d1 is a derivative of P3 with X = C. (e) Photodiode noise current vs frequency at different applied biases. The solid lines are measured values, while the dashed line was calculated from a shot noise assumption. (f) Detectivity vs incident wavelength at different applied biases. Panels (e) and (f) show data taken on a device using a 2:1 PCBM[70]/P2 blend.

prior recording frame. The caveat is that applying an external bias may trade off with the detectivity as previously discussed.

With a phototransistor, the EQE can exceed 100% through photoconductive gain, which is defined by the ratio of the trapped charge lifetime to the free carrier transit time.[44] The photoconductive gain mechanism in Figure 4d is limited in response speed, as the free carriers need time to circulate. Figure 4e,f shows the response time and frequency-dependent EQE, respectively. As the illumination frequency increased from 1 to 50 Hz, the photocurrent and EQE decreased because the light source was turned off before the electrons reached the maximum circulation, i.e., gain. There are several approaches

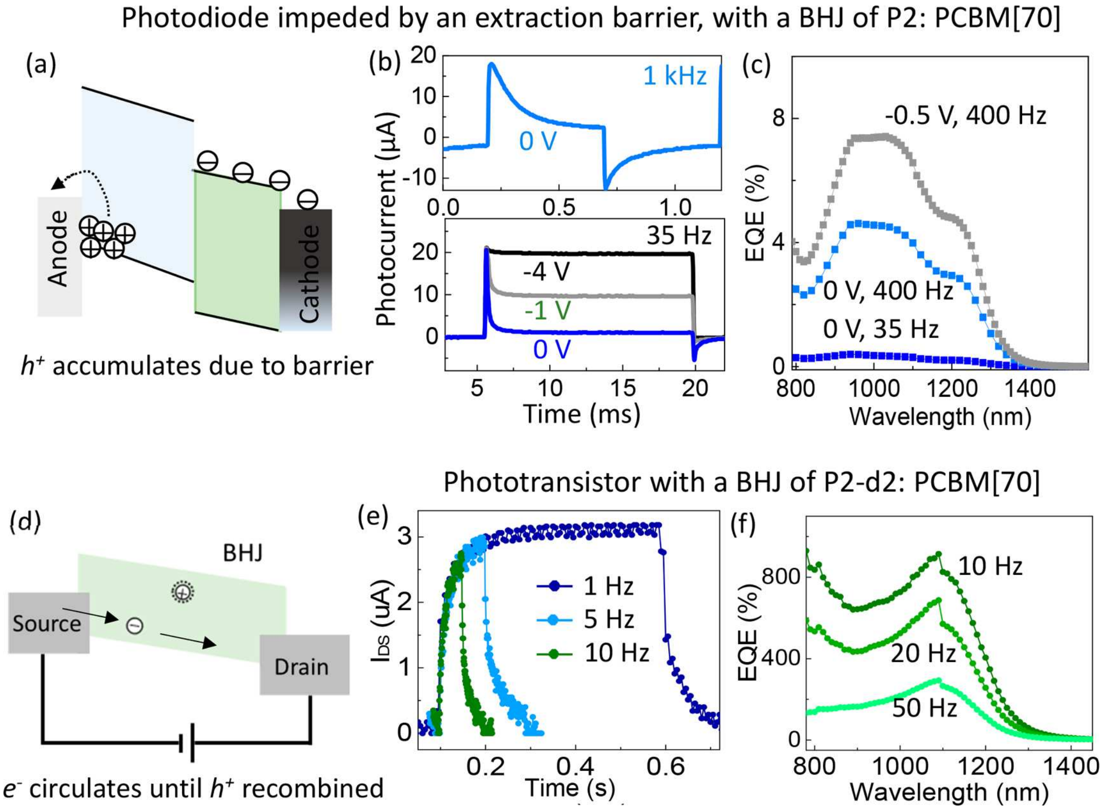

Figure 4. (a) Illustration of a charge extraction barrier due to mismatched energy levels at the electrode interface. (b) Photodiode current vs time with different biasing conditions under 1.3 mW/cm^2 illumination. The illumination time periods in this figure are labeled as frequencies at 50% duty cycle. (c) External quantum efficiency vs wavelength for various illumination frequencies and applied voltages. (d) Schematic diagram of the photoconductive gain mechanism. (e) Phototransistor source−drain current vs time for various illumination frequencies. (f) Phototransistor external quantum efficiency vs wavelength, where the incident light is pulsed at different frequencies.

to increase the response speed: (1) improve the mobility of the circulating carrier, (2) reduce the length of the transport channel, and (3) apply a higher source−drain voltage at the cost of increasing noise. We note that increasing the EQE by photoconductive gain does not necessarily translate to a higher detectivity if noise is not suppressed. To address the long response time and noise issues, rectifying junction transistors have been demonstrated to simultaneously raise the gain, bandwidth, and detectivity for SWIR colloidal dots,[45] and these structures may be applicable to organics in future photodetector development.

5. BIOAPPLICATIONS BASED ON ORGANIC INFRARED PHOTODETECTORS

Applications of organic infrared photodetectors, shown in Figure 5, encompass wearable physiological monitors to low-cost spectroscopic imagers that enable compositional analysis in food, water quality, and medical and biological studies.

5.1. Temporal Biosignals Measured by Organic Photodetectors

As illustrated in Figure 5a,b, a photoplethysmogram (PPG)[46] device can be fabricated to measure blood flow dynamics[10,24,47] and oxygenation.[11] While a body part is illuminated, the photodetector records the change in light intensity modulated by blood being pumped into and out of the body part. Thus, the PPG photocurrent tracks the heartbeat rate and variability over time, and the absorption differences at selective wavelengths form the basis for calculating blood oxygenation.

Figure 5c shows exemplar PPG signals obtained at a fingertip using our polymeric photodiodes with a near-infrared light source (λ = 980 nm). The detector resolved two peaks in each PPG cycle. The first peak (P1) was due to the heart's pumping pressure, and the second shoulder peak (P2) was due to the reflected pressure wave from the lower body.[48] As aging blood vessels become rigid and less capable of dissipating the reflected wave, the P2 peak increases and also shifts to an earlier arrival time for the reflected wave. The P2/P1 ratio is the augmentation index, which indicates arterial stiffness and is correlated with risks for heart diseases and stroke.

The demonstration in Figure 5d shows a system to measure muscle contraction and relaxation by detection of the backscattered light reflected off a bicep.[12] The backscattered light from a muscle fiber is anisotropic, and hence, changes in muscle condition can be revealed by detectors positioned along and perpendicular to the muscle fibers. The differential photosignals distinguish between shortening isotonic contractions and twisting isometric motion and complement electrophysiological measurements.[49,50]

5.2. Spectroscopic Analyses Using Organic SWIR Photodetectors

Spectroscopic analysis allows the determination of a sample's composition and is relevant to food and drug quality control. Materials common in biological tissues and drugs, such as water, lipids, and alcohol, show different absorption signatures in the SWIR. Figure 5e shows the transmission spectra of solutions with different ratios of water and ethanol, in which the transmission around λ = 1300 nm increases with a higher

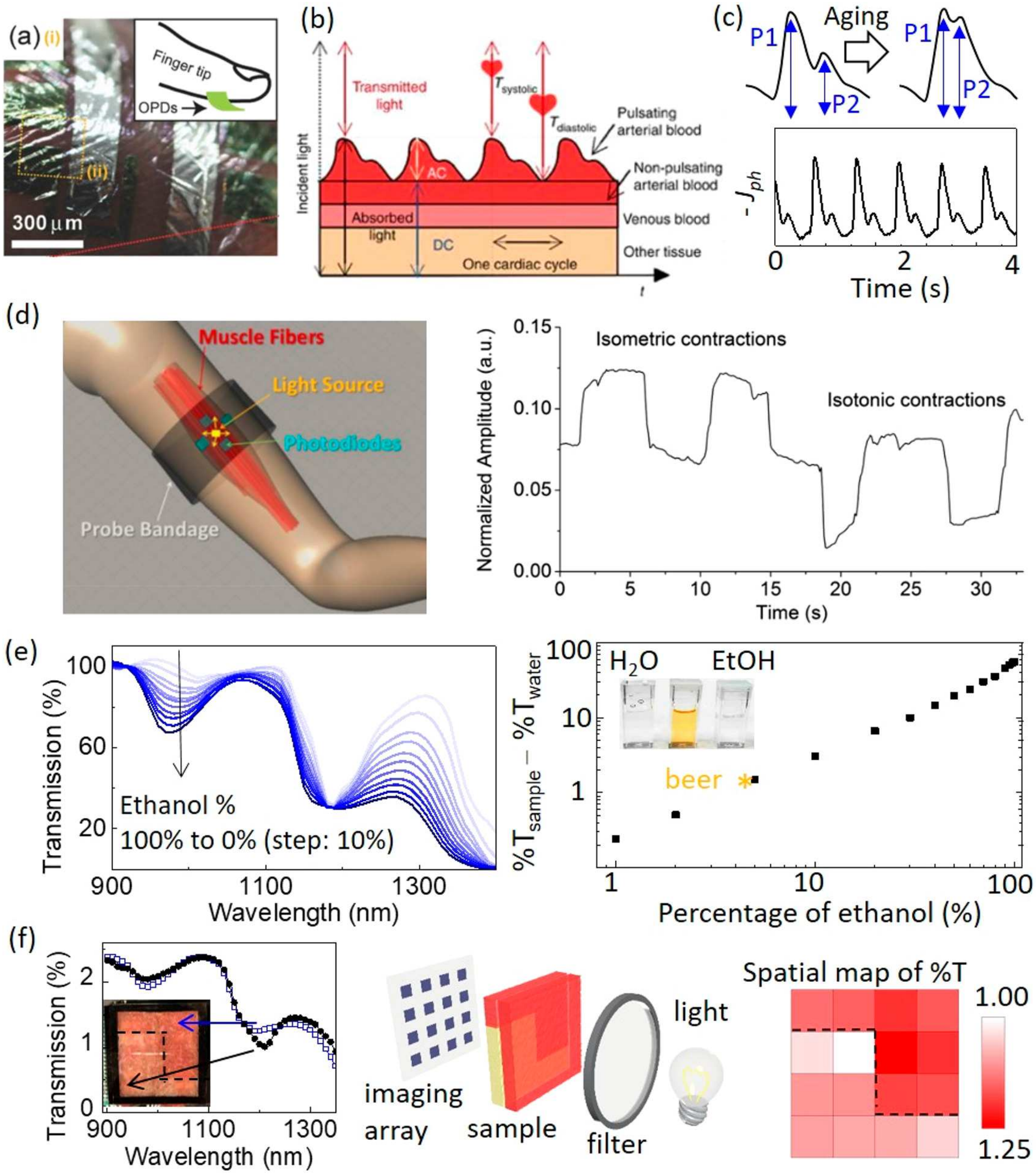

Figure 5. (a) Photograph of a conformal near-infrared photodiode on a finger. Reproduced with permission from ref 10. Copyright 2018 Wiley. (b) Schematic of a photoplethysmogram. Reproduced with permission from ref 11. Copyright 2014 Nature Publishing Group. (c) Photoplethysmogram signal detected by an organic SWIR photodiode. (d) Schematic of a muscle contraction sensor and the corresponding measurements. Reproduced from ref 12, published by Wiley. (e) Transmission spectra of ethanol solutions at varying concentrations. Reproduced with permission from ref 28. Copyright 2018 Wiley. (f) Demonstration of a noninvasive SWIR approach to analyze the fat percentage in biotissues. Reproduced with permission from ref 34. Copyright 2018 Wiley.

concentration of ethanol.[28] We can accurately identify the ethanol content in a beer sample to within 1%, and such spectroscopy is applicable to manufacturing process control of water contaminants in petroleum or alcohol excipients in medications.

Another example, in Figure 5f, utilizes the absorption difference between lean and fatty tissues at $\lambda = 1200$ nm. Here our organic SWIR photodiodes are incorporated into an active matrix array[34,51,52] that enables spatial mapping and compositional analysis to estimate fat content by noninvasive imaging. The feasibility of imaging fatty tissue will aid in diagnosis of atherosclerosis, a condition where arteries are clogged by fatty deposits, or to assist laparoscopic procedures by improving the contrast between crucial organs and surrounding fatty tissues. Organic SWIR photodiodes provide a thin, flexible form factor that is ideal for meeting space constraints in such applications.

6. SUMMARY AND OUTLOOK

SWIR photodetectors are highly desirable for bioelectronics because of the deep penetration depth of SWIR light for high-resolution, noninvasive biological imaging. Organic materials offer numerous advantages, including large-area conformal coverage, temperature insensitivity, and low-cost integration, enabling ubiquitous SWIR technologies. With the modular donor−acceptor polymers shown in Figure 2e, the device performance is rising, with detectivities exceeding 10^{11} Jones,

DOI: 10.1021/acs.accounts.8b00446
Acc. Chem. Res. 2018, 51, 3144−3153

comparable to those of commercial germanium photodiodes. The characterization efforts shown here enable us to understand the key limitations and provide a fair comparison of device performance. Novel low-band-gap organics will be investigated to aim for polymers with reduced band-tail disorder and to study blends with non-fullerene acceptors, which are promising to maximize charge transfer at negligible driving energy. Research in device structures, such as incorporating optical microcavities to increase absorption or using transistors to improve charge transport, may enhance device performance and extend spectral response. Low-cost organic SWIR technologies will be widely deployable, empowering users to discover information in the SWIR spectrum and inspire new use cases and applications.

■ AUTHOR INFORMATION

Corresponding Author

*E-mail: tnn046@ucsd.edu.

ORCID

Jason D. Azoulay: 0000-0003-0138-5961
Tse Nga Ng: 0000-0001-6967-559X

Notes

The authors declare no competing financial interest.

Biographies

Zhenghui Wu received his B.S. and Ph.D. in Physics from Hong Kong Baptist University. Since 2016 he has been a postdoctoral scholar at UCSD.

Yichen Zhai received his B.S. in Microelectronics from Changchun University of Science and Technology and his M.S. in Electrical Engineering from Stevens Institute of Technology. He is a Ph.D. student at UCSD.

Hyonwoong Kim received his B.S. and M.S. degrees in Chemical Engineering from Dankook University. He is a Ph.D. candidate at UCSD.

Jason D. Azoulay received his Ph.D. in Chemistry at the University of California Santa Barbara and joined Sandia National Laboratories as a postdoctoral appointee (2011−2014). In 2014 he was appointed as an Assistant Professor at USM.

Tse Nga Ng received her Ph.D. in Physical Chemistry at Cornell University and worked at Palo Alto Research Center for 9 years. In 2016 she was appointed as an Associate Professor in UCSD. Her group website is http://flexible-electronics.ucsd.edu.

■ ACKNOWLEDGMENTS

Z.W., Y.Z., H.K, and T.N.N. are grateful for the support from the National Science Foundation (NSF ECCS-1839361). Part of the work was performed at the San Diego Nanotechnology Infrastructure of UCSD, which is supported by NSF ECCS-1542148. J.D.A. is grateful for support from the Air Force Office of Scientific Research (Grant FA9550-17-1-0261), NSF OIA-1632825, and the Army Research Laboratory (Grant W911NF-16-2-0189).

■ REFERENCES

(1) Naczynski, D. J.; Tan, M. C.; Zevon, M.; Wall, B.; Kohl, J.; Kulesa, A.; Chen, S.; Roth, C. M.; Riman, R. E.; Moghe, P. V. Rare-Earth-Doped Biological Composites as in Vivo Shortwave Infrared Reporters. *Nat. Commun.* **2013**, *4*, 2199.

(2) Hong, G.; Diao, S.; Chang, J.; Antaris, A. L.; Chen, C.; Zhang, B.; Zhao, S.; Atochin, D. N.; Huang, P. L.; Andreasson, K. I.; Kuo, C. J.; Dai, H. Through-Skull Fluorescence Imaging of the Brain in a New near-Infrared Window. *Nat. Photonics* **2014**, *8*, 723−730.

(3) García De Arquer, F. P.; Armin, A.; Meredith, P.; Sargent, E. H. Solution-Processed Semiconductors for next-Generation Photodetectors. *Nat. Rev. Mater.* **2017**, *2*, 16100.

(4) Dou, L.; Liu, Y.; Hong, Z.; Li, G.; Yang, Y. Low-Bandgap Near-IR Conjugated Polymers/Molecules for Organic Electronics. *Chem. Rev.* **2015**, *115*, 12633−12665.

(5) Ng, T. N.; Wong, W. S.; Lujan, R. A.; Street, R. A. Characterization of Charge Collection in Photodiodes under Mechanical Strain: Comparison between Organic Bulk Heterojunction and Amorphous Silicon. *Adv. Mater.* **2009**, *21*, 1855−1859.

(6) Wang, S.; Oh, J. Y.; Xu, J.; Tran, H.; Bao, Z. Skin-Inspired Electronics: An Emerging Paradigm. *Acc. Chem. Res.* **2018**, *51*, 1033−1045.

(7) Root, S. E.; Savagatrup, S.; Printz, A. D.; Rodriquez, D.; Lipomi, D. J. Mechanical Properties of Organic Semiconductors for Stretchable, Highly Flexible, and Mechanically Robust Electronics. *Chem. Rev.* **2017**, *117*, 6467−6499.

(8) Ready, S.; Endicott, F.; Whiting, G. L.; Ng, T. N.; Chow, E. M.; Lu, J. 3D Printed Electronics. *NIP Digital Fabr. Conf.* **2013**, *2013*, 9−12.

(9) Inal, S.; Rivnay, J.; Suiu, A.-O.; Malliaras, G. G.; McCulloch, I. Conjugated Polymers in Bioelectronics. *Acc. Chem. Res.* **2018**, *51*, 1368−1376.

(10) Park, S.; Fukuda, K.; Wang, M.; Lee, C.; Yokota, T.; Jin, H.; Jinno, H.; Kimura, H.; Zalar, P.; Matsuhisa, N.; Umezu, S.; Bazan, G. C.; Someya, T. Ultraflexible Near-Infrared Organic Photodetectors for Conformal Photoplethysmorgram Sensors. *Adv. Mater.* **2018**, *30*, 1802359.

(11) Lochner, C. M.; Khan, Y.; Pierre, A.; Arias, A. C. All-Organic Optoelectronic Sensor for Pulse Oximetry. *Nat. Commun.* **2014**, *5*, 5745.

(12) Bansal, A. K.; Hou, S.; Kulyk, O.; Bowman, E. M.; Samuel, I. D. W. Wearable Organic Optoelectronic Sensors for Medicine. *Adv. Mater.* **2015**, *27*, 7638−7644.

(13) Lee, Y. H.; Kweon, O. Y.; Kim, H.; Yoo, J. H.; Han, S. G.; Oh, J. H. Recent Advances in Organic Sensors for Health Self-Monitoring Systems. *J. Mater. Chem. C* **2018**, *6*, 8569−8612.

(14) Gong, X.; Tong, M.; Xia, Y.; Cai, W.; Moon, J. S.; Cao, Y.; Yu, G.; Shieh, C.-L.; Nilsson, B.; Heeger, A. J. High-Detectivity Polymer Photodetectors with Spectral Response from 300 nm to 1450 nm. *Science* **2009**, *325*, 1665−1667.

(15) Han, J.; Yang, D.; Ma, D.; Qiao, W.; Wang, Z. Y. Low-Bandgap Polymers for High-Performance Photodiodes with Maximal EQE near 1200 nm and Broad Spectral Response from 300 to 1700 nm. *Adv. Opt. Mater.* **2018**, *6*, 1800038.

(16) Zimmerman, J. D.; Diev, V. V.; Hanson, K.; Lunt, R. R.; Yu, E. K.; Thompson, M. E.; Forrest, S. R. Porphyrin-Tape/C_{60} Organic Photodetectors with 6.5% External Quantum Efficiency in the Near Infrared. *Adv. Mater.* **2010**, *22*, 2780−2783.

(17) Young, M.; Suddard-Bangsund, J.; Patrick, T. J.; Pajares, N.; Traverse, C. J.; Barr, M. C.; Lunt, S. Y.; Lunt, R. R. Photovoltaic Devices: Organic Heptamethine Salts for Photovoltaics and Detectors with Near-Infrared Photoresponse up to 1600 nm. *Adv. Opt. Mater.* **2016**, *4*, 1027.

(18) London, A. E.; Huang, L.; Zhang, B.; Oviedo, B.; Tropp, J.; Yao, W.; Wu, Z.; Wong, B.; Ng, T. N.; Azoulay, J. D. Donor−Acceptor Polymers with Tunable Infrared Photoresponse. *Polym. Chem.* **2017**, *8*, 2922−2930.

(19) Hendriks, K. H.; Li, W.; Wienk, M. M.; Janssen, R. A. J. Small-Bandgap Semiconducting Polymers with High Near-Infrared Photoresponse. *J. Am. Chem. Soc.* **2014**, *136*, 12130−12136.

(20) Arnold, M. S.; Zimmerman, J. D.; Renshaw, C. K.; Xu, X.; Lunt, R. R.; Austin, C. M.; Forrest, S. R. Broad Spectral Response Using Carbon Nanotube/Organic Semiconductor/C_{60} Photodetectors. *Nano Lett.* **2009**, *9*, 3354−3358.

DOI: 10.1021/acs.accounts.8b00446

(21) Zheng, L.; Zhu, T.; Xu, W.; Liu, L.; Zheng, J.; Gong, X.; Wudl, F. Solution-Processed Broadband Polymer Photodetectors with Spectral Response Up to 2.5 um by a Low Bandgap Donor-Acceptor Conjugated Copolymer. *J. Mater. Chem. C* **2018**, *6*, 3634−3641.

(22) Nachabé, R.; Hendriks, B. H. W.; van der Voort, M.; Desjardins, A. E.; Sterenborg, H. J. C. M. Estimation of Biological Chromophores Using Diffuse Optical Spectroscopy: Benefit of Extending the UV-VIS Wavelength Range to Include 1000 to 1600 nm. *Biomed. Opt. Express* **2010**, *1*, 1432.

(23) Wilson, R. H.; Nadeau, K. P.; Jaworski, F. B.; Tromberg, B. J.; Durkin, A. J. Review of Short-Wave Infrared Spectroscopy and Imaging Methods for Biological Tissue Characterization. *J. Biomed. Opt.* **2015**, *20*, 030901.

(24) Wu, Z.; Yao, W.; London, A. E.; Azoulay, J. D.; Ng, T. N. Temperature-Dependent Detectivity of Near-Infrared Organic Bulk Heterojunction Photodiodes. *ACS Appl. Mater. Interfaces* **2017**, *9*, 1654−1660.

(25) Rauch, T.; Boberl, M.; Tedde, S. F.; Furst, J.; Kovalenko, M. V.; Hesser, G. G.; Lemmer, U.; Heiss, W.; Hayden, O. Near-Infrared Imaging with Quantum-Dot-Sensitized Organic Photodiodes. *Nat. Photonics* **2009**, *3*, 332−336.

(26) Lee, J. W.; Kim, D. Y.; Baek, S.; Yu, H.; So, F. Inorganic UV-Visible-SWIR Broadband Photodetector Based on Monodisperse PbS Nanocrystals. *Small* **2016**, *12*, 1328−1333.

(27) Tang, Z.; Ma, Z.; Sánchez-Díaz, A.; Ullbrich, S.; Liu, Y.; Siegmund, B.; Mischok, A.; Leo, K.; Campoy-Quiles, M.; Li, W.; Vandewal, K. Polymer:Fullerene Bimolecular Crystals for Near-Infrared Spectroscopic Photodetectors. *Adv. Mater.* **2017**, *29*, 1702184.

(28) Wu, Z.; Yao, W.; London, A. E.; Azoulay, J. D.; Ng, T. N. Elucidating the Detectivity Limits in Shortwave Infrared Organic Photodiodes. *Adv. Funct. Mater.* **2018**, *28*, 1800391.

(29) Sulas, D. B.; London, A. E.; Huang, L.; Xu, L.; Wu, Z.; Ng, T. N.; Wong, B. M.; Schlenker, C. W.; Azoulay, J. D.; Sfeir, M. Y. Preferential Charge Generation at Aggregate Sites in Narrow Band Gap Infrared Photoresponsive Polymer Semiconductors. *Adv. Opt. Mater.* **2018**, *6*, 1701138.

(30) Jansen-van Vuuren, R. D.; Armin, A.; Pandey, A. K.; Burn, P. L.; Meredith, P. Organic Photodiodes: The Future of Full Color Detection and Image Sensing. *Adv. Mater.* **2016**, *28*, 4766−4802.

(31) Baeg, K. J.; Binda, M.; Natali, D.; Caironi, M.; Noh, Y. Y. Organic Light Detectors: Photodiodes and Phototransistors. *Adv. Mater.* **2013**, *25*, 4267−4295.

(32) Gasparini, N.; Wadsworth, A.; Moser, M.; Baran, D.; McCulloch, I.; Brabec, C. J. The Physics of Small Molecule Acceptors for Efficient and Stable Bulk Heterojunction Solar Cells. *Adv. Energy Mater.* **2018**, *8*, 1703298.

(33) Hou, J.; Inganäs, O.; Friend, R. H.; Gao, F. Organic Solar Cells Based on Non-Fullerene Acceptors. *Nat. Mater.* **2018**, *17*, 119−128.

(34) Wu, Z.; Zhai, Y.; Yao, W.; Eedugurala, N.; Zhang, S.; Huang, L.; Gu, X.; Azoulay, J. D.; Ng, T. N. The Role of Dielectric Screening in Organic Shortwave Infrared Photodiodes for Spectroscopic Image Sensing. *Adv. Funct. Mater.* **2018**, *28*, 1805738.

(35) Ng, T. N.; Fujieda, I.; Street, R. A.; Veres, J. Persistent Photoconductivity Effects in Printed N-Channel Organic Transistors. *J. Appl. Phys.* **2013**, *113*, 094506.

(36) Ng, T. N.; Schwartz, D. E.; Mei, P.; Krusor, B.; Kor, S.; Veres, J.; Bröms, P.; Eriksson, T.; Wang, Y.; Hagel, O.; Karlsson, C. Printed Dose-Recording Tag Based on Organic Complementary Circuits and Ferroelectric Nonvolatile Memories. *Sci. Rep.* **2015**, *5*, 13457.

(37) Paterson, A. F.; Singh, S.; Fallon, K. J.; Hodsden, T.; Han, Y.; Schroeder, B. C.; Bronstein, H.; Heeney, M.; McCulloch, I.; Anthopoulos, T. D. Recent Progress in High-Mobility Organic Transistors: A Reality Check. *Adv. Mater.* **2018**, *30*, 1801079.

(38) Rim, Y. S.; Yang, Y. M.; Bae, S.; Chen, H.; Li, C.; Goorsky, M. S.; Yang, Y. Ultrahigh and Broad Spectral Photodetectivity of an Organic − Inorganic Hybrid Phototransistor for Flexible Electronics. *Adv. Mater.* **2015**, *27*, 6885−6891.

(39) Kim, H.; Ng, T. N. Reducing Trap States in Printed Indium Zinc Oxide Transistors by Doping with Benzyl Viologen. *Adv. Electronic Mater.* **2018**, *4*, 1700631.

(40) Benduhn, J.; Tvingstedt, K.; Piersimoni, F.; Ullbrich, S.; Fan, Y.; Tropiano, M.; McGarry, K. A.; Zeika, O.; Riede, M. K.; Douglas, C. J.; Barlow, S.; Marder, S. R.; Neher, D.; Spoltore, D.; Vandewal, K. Intrinsic Non-Radiative Voltage Losses in Fullerene-Based Organic Solar Cells. *Nature Energy* **2017**, *2*, 17053.

(41) Vandewal, K.; Albrecht, S.; Hoke, E. T.; Graham, K. R.; Widmer, J.; Douglas, J. D.; Schubert, M.; Mateker, W. R.; Bloking, J. T.; Burkhard, G. F.; Sellinger, A.; Frechet, J. M.; Amassian, A.; Riede, M. K.; McGehee, M.; Neher, D.; Salleo, A. Efficient Charge Generation by Relaxed Charge-Transfer States at Organic Interfaces. *Nat. Mater.* **2014**, *13*, 63−68.

(42) Street, R. A.; Krakaris, A.; Cowan, S. R. Recombination through Different Types of Localized States in Organic Solar Cells. *Adv. Funct. Mater.* **2012**, *22*, 4608−4619.

(43) Guerrero, A.; Loser, S.; Garcia-Belmonte, G.; Bruns, C. J.; Smith, J.; Miyauchi, H.; Stupp, S. I.; Bisquert, J.; Marks, T. J. Solution-Processed Small Molecule:Fullerene Bulk-Heterojunction Solar Cells: Impedance Spectroscopy Deduced Bulk and Interfacial Limits to Fill-Factors. *Phys. Chem. Chem. Phys.* **2013**, *15*, 16456−16462.

(44) Lee, J. W.; Kim, D. Y.; So, F. Unraveling the Gain Mechanism in High Performance Solution-Processed PbS Infrared PIN Photodiodes. *Adv. Funct. Mater.* **2015**, *25*, 1233−1238.

(45) Adinolfi, V.; Sargent, E. H. Photovoltage Field-Effect Transistors. *Nature* **2017**, *542*, 324−327.

(46) Sun, Y.; Thakor, N. Photoplethysmography Revisited: From Contact to Noncontact, from Point to Imaging. *IEEE Trans. Biomed. Eng.* **2016**, *63*, 463−477.

(47) Zhai, Y.; Lee, J.; Hoang, Q.; Sievenpipper, D.; Garudadri, H.; Ng, T. N. Printed Wireless Fluidic Pressure Sensor. *Flexible Printed Electron.* **2018**, *3*, 035006.

(48) Allen, J.; Murray, A. Age-Related Changes in the Characteristics of the Photoplethysmographic Pulse Shape at Various Body Sites. *Physiological Measurement* **2003**, *24*, 297−307.

(49) Wang, K.; Parekh, U.; Pailla, T.; Garudadri, H.; Gilja, V.; Ng, T. N. Stretchable Dry Electrodes with Concentric Ring Geometry for Enhancing Spatial Resolution in Electrophysiology. *Adv. Healthcare Mater.* **2017**, *6*, 1700552.

(50) Fang, H.; Yu, K. J.; Gloschat, C.; Yang, Z.; Song, E.; Chiang, C. H.; Zhao, J.; Won, S. M.; Xu, S.; Trumpis, M.; Zhong, Y.; Han, S. W.; Xue, Y.; Xu, D.; Choi, S. W.; Cauwenberghs, G.; Kay, M.; Huang, Y.; Viventi, J.; Efimov; Rogers, J. A. Capacitively Coupled Arrays of Multiplexed Flexible Silicon Transistors for Long-Term Cardiac Electrophysiology. *Nature Biomedical Engineering* **2017**, *1*, 0038.

(51) Ng, T. N.; Wong, W. S.; Chabinyc, M. L.; Sambandan, S.; Street, R. A. Flexible Image Sensor Array with Bulk Heterojunction Organic Photodiode. *Appl. Phys. Lett.* **2008**, *92*, 213303.

(52) Gelinck, G. H.; Kumar, A.; Moet, D.; van der Steen, J.-L. P. J.; van Breemen, A. J. J. M.; Shanmugam, S.; Langen, A.; Gilot, J.; Groen, P.; Andriessen, R.; Simon, M.; Ruetten, W.; Douglas, A. U.; Raaijmakers, R.; Malinowski, P. E.; Myny, K. X-Ray Detector-on-Plastic With High Sensitivity Using Low Cost, Solution-Processed Organic Photodiodes. *IEEE Trans. Electron Devices* **2016**, *63*, 197−204.

■ NOTE ADDED AFTER ASAP PUBLICATION

This paper published ASAP on December 06, 2018 with an error in Figure 3. The revised paper was reposted on December 7, 2018.